J|A|C|S ARTICLES

Published on Web 03/03/2010

Elucidation of the Self-Assembly Pathway of Lanreotide Octapeptide into β-Sheet Nanotubes: Role of Two Stable Intermediates

Emilie Pouget,[†,+] Nicolas Fay,[‡] Erik Dujardin,[§] Nadège Jamin,[‡] Patrick Berthault,[||] Lionel Perrin,[‡,%] Anjali Pandit,[‡,○] Thierry Rose,[⊥] Céline Valéry,[#] Daniel Thomas,[▽] Maïté Paternostre,*[,‡] and Franck Artzner*[,†]

Institut de Physique de Rennes, UMR 6251 CNRS & Université Rennes 1, 263 Avenue du général Leclerc, F-35042 Rennes Cedex, France, CEA, iBiTec-S, Service de Bioénergétique Biologie Structurale et Mécanismes (SB^{2}SM) and CNRS, URA 2096, CEA-Saclay, F-91191 Gif-sur-Yvette, France, NanoSciences Group, CEMES UPR 8011 CNRS, BP 94347, 29 rue J. Marvig, F-31055 Toulouse Cedex 4, France, CEA, IRAMIS, Service interdisciplinaire sur les systèmes moléculaires et les matériaux, Laboratoire Structure et Dynamique par Résonance Magnétique, URA CEA/CNRS 331, 91191 Gif-sur-Yvette, France, Institut Pasteur, Plate-Forme de Biophysique des Macromolécules et de leurs Interactions, 25 rue du Dr Roux, F-75724 Paris Cedex 15, France, Ipsen Pharma S.A., Ctra. Laurea Miro 395, 08980-Sant Feliu de Llobregat, Barcelona, Spain, and Interactions Cellulaires et Moléculaires, UMR 6026 CNRS & Université Rennes 1, 263 Avenue du général Leclerc, F-35042 Rennes Cedex, France

Received October 21, 2009; E-mail: maite.paternostre@cea.fr; franck.artzner@univ-rennes1.fr

Abstract: Nanofabrication by molecular self-assembly involves the design of molecules and self-assembly strategies so that shape and chemical complementarities drive the units to organize spontaneously into the desired structures. The power of self-assembly makes it the ubiquitous strategy of living organized matter and provides a powerful tool to chemists. However, a challenging issue in the self-assembly of complex supramolecular structures is to understand how kinetically efficient pathways emerge from the multitude of possible transition states and routes. Unfortunately, very few systems provide an intelligible structure and formation mechanism on which new models can be developed. Here, we elucidate the molecular and supramolecular self-assembly mechanism of synthetic octapeptide into nanotubes in equilibrium conditions. Their complex hierarchical self-assembly has recently been described at the mesoscopic level, and we show now that this system uniquely exhibits three assembly stages and three intermediates: (i) a peptide dimer is evidenced by both analytical centrifugation and NMR translational diffusion experiments; (ii) an open ribbon and (iii) an unstable helical ribbon are both visualized by transmission electron microscopy and characterized by small angle X-ray scattering. Interestingly, the structural features of two stable intermediates are related to the final nanotube organization as they set, respectively, the nanotube wall thickness and the final wall curvature radius. We propose that a specific self-assembly pathway is selected by the existence of such preorganized and stable intermediates so that a unique final molecular organization is kinetically favored. Our findings suggests that the rational design of oligopeptides can encode both molecular- and macro-scale morphological characteristics of their higher-order assemblies, thus opening the way to ultrahigh resolution peptide scaffold engineering.

Introduction

Nanofabrication of complex form by molecular self-assembly involves the design of molecules and self-assembly strategies so that shape and chemical complementarities drive the units to organize spontaneously into the desired structures. The power of self-assembly makes it the ubiquitous strategy of organized living matter and provides a powerful tool to chemists. Indeed, (i) modern synthetic chemistry can design building blocks with an atomic precision unattainable by other nanofabrication approaches, (ii) self-assembly schemes can be inspired by the wealth of biological examples, (iii) biocompatibility of the final architectures can be envisioned, and (iv) kinetically biased and thermodynamically stable structures can be obtained by controlling the formation equilibria leading to defect-free or even self-healing constructions.

[†] UMR 6251 CNRS & Université Rennes 1.
[‡] CEA, iBiTec-S.
[§] CEMES UPR 8011 CNRS.
[||] CEA, IRAMIS.
[⊥] Institut Pasteur.
[#] Ipsen Pharma S.A.
[▽] UMR 6026 CNRS & Université Rennes 1.
[+] Current address: Structure et dynamique de macromolécules biologiques, CRPP, 115 Avenue Schweitzer 33600 Pessac, FRANCE.
[%] Current address: Laboratoire de Physique et Chimie des Nano-Objets, UMR 5215, INSA/UPS/CNRS, 135 Avenue de Rangueil, 31077 Toulouse Cedex 4, France.
[○] Current address: Leiden Institute of Chemistry, LCP 103, Leiden University, PO Box 9502, 2300 RA Leiden, The Netherlands.

10.1021/ja9088023

For these reasons, self-assemblies processes are the focal point of a vast multidisciplinary effort of research from the understanding of their contribution to the biological machinery to the construction of multifunctional bionanotechnological systems via the creation of new supramolecular architectures. In particular, the dynamic properties of self-assembled complex architectures have attracted specific attention recently. For example, protein self-assemblies made of actin filaments, microtubules, and intermediate filaments, collectively known as the cytoskeleton, not only account for the shapes of living cells but also control their deformation and ensure the cells' growth, division, and movements as well as active intracellular transport. Similarly, the protection of the genetic information is ensured by the reversible compaction of DNA by histone proteins, and the expression of the genetic information is controlled by dynamically self-assembled macrocomplexes of proteins.

The exquisite precision and awesome complexity of such natural systems has therefore stimulated synthetic "bottom-up" approaches to the self-assembly of molecular building blocks, such as lipids, DNA- and RNA-derived synthetic molecules, or proteins, into novel well-defined nanostructures. For small lipidic molecules, the morphological control mostly consists of the deformation of molecular sheets into twisted or helical ribbons or nanotubes.[1] Recently, the sequence design and functionalization of nucleic acids allowed the self-assembly of arbitrarily complex 2D patterns[2] and even 3D Archimedean solids.[3−5] Such organic constructions have gained interest as templates able to organize or nucleate inorganic nanoparticles[4,6−8] in order to pattern physical properties with truly nanometer scale resolution, with potentials in nonconventional information processing. It is worthwhile to note that protein and peptide self-assemblies have already been applied and commercialized in drug delivery.[9]

Meanwhile, proteins are certainly providing the most advanced tools for bioinspired nanotechnologies since the first successful in vitro reconstitution of viral capsids from isolated proteins of tobacco mosaic virus (TMV).[10] In general, the in vitro reassembly of proteins produces architectures that exhibit the same molecular and supramolecular structures as their in vivo counterparts,[11,12] indicating that self-assembly derives from a thermodynamic equilibrium defined by external conditions such as ionic strength, temperature, or pH. However, the thorough understanding of the molecular structure of such architectures and of the molecular processes and physicochemical parameters driving their nucleation and growth are hampered by the scarcity of natural or synthetic systems known to date. It is worth mentioning that only very recently a molecular model has been proposed for the atomic structure of actin filaments.[13] Similarly, molecular scale structures of fibers produced from synthetic peptides,[14−16] lipids,[17−19] cholesterol, and bile salts[20,21] were recently reported.

Interestingly, the influence of protein folding and misfolding on the formation mechanisms of amyloid fibers has been elucidated[22,23] and observed later on for other proteins, sparking the idea that any protein can potentially undergo fibrillation, provided that adequate physicochemical conditions are applied.[24−28] The interplay between the dynamics, stability, and function of supramolecular complexes at the molecular level is a challenging issue, which has been elucidated for only a few systems, namely, the microtubules,[29−31] the actin filaments,[13,32] and the TMV capsid.[12,33] Most other complex biological systems do not provide an easy access to molecular and physicochemical parameters driving their self-assembly. For example, the low solubility of gas vesicle proteins prevents in vitro reassembly of the oligomeric intermediate states leading to the final architectures, de facto restricting the studies to the structure and protein packing in the final vesicle walls.[34,35] Furthermore, the

(1) Selinger, J. V.; Spector, M. S.; Schnur, J. M. *J. Phys. Chem. B* **2001**, *105*, 7157–7169.
(2) Rothemund, P. W. K. *Nature* **2006**, *440*, 297–302.
(3) Chen, J. H.; Seeman, N. C. *Nature* **1991**, *350*, 631–633.
(4) Zhang, Y. W.; Seeman, N. C. *J. Am. Chem. Soc.* **1994**, *116*, 1661–1669.
(5) Shih, W. M.; Quispe, J. D.; Joyce, G. F. *Nature* **2004**, *427*, 618–621.
(6) Le, J. D.; Pinto, Y.; Seeman, N. C.; Musier-Forsyth, K.; Taton, T. A.; Kiehl, R. A. *Nano Lett.* **2004**, *4*, 2343–2347.
(7) Banerjee, I. A.; Yu, L. T.; Matsui, H. *J. Am. Chem. Soc.* **2005**, *127*, 16002–16003.
(8) Sharma, J.; Ke, Y. G.; Lin, C. X.; Chhabra, R.; Wang, Q. B.; Nangreave, J.; Liu, Y.; Yan, H. *Angew. Chem., Int. Ed.* **2008**, *47*, 5157–5159.
(9) Zhao, F.; Ma, M. L.; Xu, B. *Chem. Soc. Rev.* **2009**, *38*, 883–891.
(10) Fraenkel-Conrat, H.; Williams, R. C. *Proc. Natl. Acad. Sci. U.S.A.* **1955**, *41*, 690–698.
(11) Weisenberg, R. C. *Science* **1972**, *177*, 1104–1105.
(12) Klug, A. *Philos. Trans. R. Soc. London, Ser. B* **1999**, *354*, 531–535.
(13) Oda, T.; Iwasa, M.; Aihara, T.; Maeda, Y.; Narita, A. *Nature* **2009**, *457*, 441–445.
(14) Serpell, L. C.; Blake, C. C. F.; Fraser, P. E. *Biochemistry* **2000**, *39*, 13269–13275.
(15) Valery, C.; Paternostre, M.; Robert, B.; Gulik-Krzywicki, T.; Narayanan, T.; Dedieu, J. C.; Keller, G.; Torres, M. L.; Cherif-Cheikh, R.; Calvo, P.; Artzner, F. *Proc. Natl. Acad. Sci. U.S.A.* **2003**, *100*, 10258–10262.
(16) Papanikolopoulou, K.; Schoehn, G.; Forge, V.; Forsyth, V. T.; Riekel, C.; Hernandez, J. F.; Ruigrok, R. W. H.; Mitraki, A. *J. Biol. Chem.* **2005**, *280*, 2481–2490.
(17) Yui, H.; Minamikawa, H.; Danev, R.; Nagayama, K.; Kamiya, S.; Shimizu, T. *Langmuir* **2008**, *24*, 709–713.
(18) Brizard, A.; Aime, C.; Labrot, T.; Huc, I.; Berthier, D.; Artzner, F.; Desbat, B.; Oda, R. *J. Am. Chem. Soc.* **2007**, *129*, 3754–3762.
(19) Oda, R.; Artzner, F.; Laguerre, M.; Huc, I. *J. Am. Chem. Soc.* **2008**, *130*, 14705–14712.
(20) Zastavker, Y. V.; Asherie, N.; Lomakin, A.; Pande, J.; Donovan, J. M.; Schnur, J. M.; Benedek, G. B. *Proc. Natl. Acad. Sci. U.S.A.* **1999**, *96*, 7883–7887.
(21) Khaykovich, B.; Hossain, C.; McManus, J. J.; Lomakin, A.; Moncton, D. E.; Benedek, G. B. *Proc. Natl. Acad. Sci. U.S.A.* **2007**, *104*, 9656–9660.
(22) Pan, K. M.; Baldwin, M.; Nguyen, J.; Gasset, M.; Serban, A.; Groth, D.; Mehlhorn, I.; Huang, Z. W.; Fletterick, R. J.; Cohen, F. E.; Prusiner, S. B. *Proc. Natl. Acad. Sci. U.S.A.* **1993**, *90*, 10962–10966.
(23) Prusiner, S. B. *Proc. Natl. Acad. Sci. U.S.A.* **1998**, *95*, 13363–13383.
(24) Jimenez, J. L.; Nettleton, E. J.; Bouchard, M.; Robinson, C. V.; Dobson, C. M.; Saibil, H. R. *Proc. Natl. Acad. Sci. U.S.A.* **2002**, *99*, 9196–9201.
(25) Johnson, R. J.; Christodoulou, J.; Dumoulin, M.; Caddy, G. L.; Alcocer, M. J.; Murtagh, G. J.; Kumita, J. R.; Larsson, G.; Robinson, C. V.; Archer, D. B.; Luisi, B.; Dobson, C. M. *J. Mol. Biol.* **2005**, *352*, 823–836.
(26) Fandrich, M.; Fletcher, M. A.; Dobson, C. M. *Nature* **2001**, *410*, 165–166.
(27) van Grondelle, W.; Iglesias, C. L.; Coll, E.; Artzner, F.; Paternostre, M.; Lacombe, F.; Cardus, M.; Martinez, G.; Montes, M.; Cherif-Cheikh, R.; Valery, C. *J. Struct. Biol.* **2007**, *160*, 211–223.
(28) Maji, S. K.; Perrin, M. H.; Sawaya, M. R.; Jessberge, S.; Vadodaria, K.; Rissman, R. A.; Singru, P. S.; Nilsson, K. P. R.; Simon, R.; David, S.; Eisenberg, D.; Rivier, J.; Sawchenko, P.; Vale, W.; Riek, R. *Science* **2009**, 328–332. .
(29) Mandelkow, E.; Song, Y. H.; Schweers, O.; Marx, A.; Mandelkow, E. M. *Neurobiol. Aging* **1995**, *16*, 347–354.
(30) Nogales, E.; Wolf, S. G.; Downing, K. H. *Nature* **1998**, *393*, 191–191.
(31) Chretien, D.; Fuller, S. D.; Karsenti, E. *J. Cell Biol.* **1995**, *129*, 1311–1328.
(32) Korn, E. D.; Carlier, M. F.; Pantaloni, D. *Science* **1987**, *238*, 638–644.
(33) Caspar, D. L. D. *Adv. Protein Chem.* **1963**, *18*, 37–121.
(34) Blaurock, A. E.; Wober, W. *J. Mol. Biol.* **1976**, *106*, 871–888.

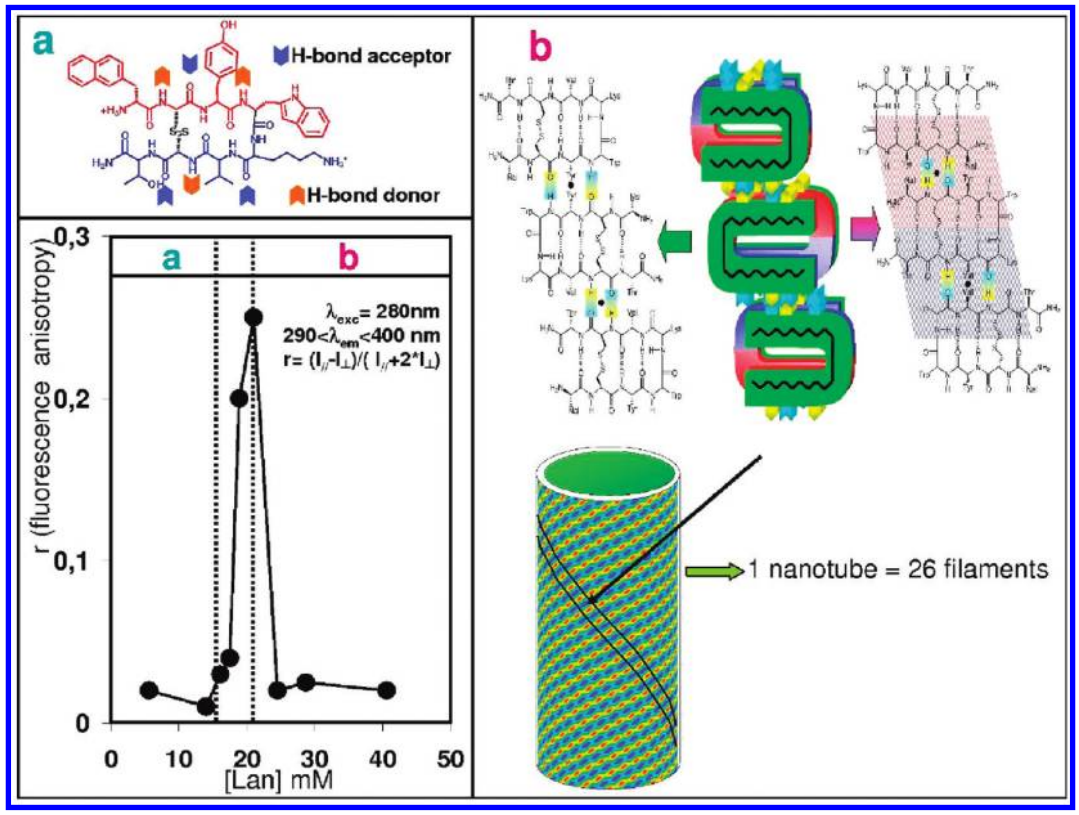

Figure 1. Fluorescence anisotropy versus lanreotide concentration. (a) The lanreotide molecule: (NH_3^+-D-2-Nal-cyclo-[Cys-Tyr-D-Trp-Lys-Val-Cys]-Thr-$CONH_2$). Aromatic and aliphatic portions are red and blue respectively. The H-bond donor (red) and acceptor (blue) groups free for intermolecular interaction are represented. (b) Molecular and supramolecular stacking of lanreotide in the nanotube wall as described by Valery at al.[15] Color code: green, hydrophilic; red, aromatic hydrophobic; and blue, aliphatic hydrophobic surface of the peptide. Panels a and b were adapted from ref 15 (Copyright 2003 National Academy of Sciences, U.S.A.). (Lower left panel) Evolution of the fluorescence anisotropy of lanreotide with concentration in water. The dotted lines on the figure underline three concentration domains: domain a (characterized by the nonassembled peptides) and domain b (characterized by the peptide nanotubes) separated by an intermediate concentration domain.

self-assembly kinetics are typically very slow or very fast depending on the growth phase, making it difficult to observe the processes in equilibrium conditions. The in vitro formation of amyloid fibres results from a very slow nucleation stage followed by a very fast fiber elongation. These inherent difficulties are further amplified by the existence of concomitant pathways leading to different fiber morphologies that have been either experimentally observed[36] or predicted by molecular dynamics.[37−39] As a result, the deciphering of the molecular and supramolecular pathways toward complex self-assembly is exceedingly complicated[40] and has been rarely elucidated by the observations of stable intermediates.[41,42]

This context generates a high expectation for model yet realistic bioinspired systems well-suited for the study of elementary self-assembly mechanisms leading to complex architectures with an experimental access to each intermediate molecular moiety. A partial answer to this challenge has been given in the cases of lipid-like peptides self-assembled into curved lamellae and nanotubes that mimic the spatial separation in cells[43] and of β-amyloid peptides that reproduce the self-assembly properties of the entire protein.[44,45]

In the present work, for the first time we fully elucidate three successive steps of the self-assembly process of a somatostatine octapeptide analogue, lanreotide, into nanotubes. Lanreotide (Figure 1a) self-assembles reversibly into micrometer-long, hollow nanotubes with a rigorously monodisperse diameter (24.4 nm).[15] The molecular and supramolecular packing of the peptide within the nanotubes exhibits as much as four levels of ordering. The nanotubes are organized in a hexagonal lattice. The wall is formed by the packing of lanreotide in a 2-D monoclinic lattice with $i = 20.7$ Å, $j = 20.8$ Å, $\gamma = 117.2°$. The j vector, which is at an angle of 48.3° with respect to the direction of the cylinder axis, is due to an antiparallel H-bound network. The wall thickness of 18 Å implies that the building block of the nanotubes is a dimer. Moreover, due to a systematic segregation of the aromatic moiety of the molecule, it is a face to face dimer. This highly hierarchical organization is unique in the field of

(35) Blaurock, A. E.; Walsby, A. E. *J. Mol. Biol.* **1976**, *105*, 183–199.
(36) Goldsbury, C.; Frey, P.; Olivieri, V.; Aebi, U.; Muller, S. A. *J. Mol. Biol.* **2005**, *352*, 282–298.
(37) Zheng, J.; Jang, H.; Nussinov, R. *Biochemistry* **2008**, *47*, 2497–2509.
(38) Bellesia, G.; Shea, J. E. *J. Chem. Phys.* **2009**, *131*, 111102–111106.
(39) Pellarin, R.; Guarnera, E.; Caflisch, A. *J. Mol. Biol.* **2007**, *374*, 917–924.
(40) Teplow, D. B.; Lazo, N. D.; Bitan, G.; Bernstein, S.; Wyttenbach, T.; Bowers, M. T.; Baumketner, A.; Shea, J. E.; Urbanc, B.; Cruz, L.; Borreguero, J.; Stanley, H. E. *Acc. Chem. Res.* **2006**, *39*, 635–645.
(41) Aggeli, A.; Nyrkova, I. A.; Bell, M.; Harding, R.; Carrick, L.; McLeish, T. C.; Semenov, A. N.; Boden, N. *Proc. Natl. Acad. Sci. U.S.A.* **2001**, *98*, 11857–11862.
(42) Marini, D. M.; Hwang, W.; Lauffenburger, D. A.; Zhang, S. G.; Kamm, R. D. *Nano Lett.* **2002**, *2*, 295–299.
(43) Yang, Y. L.; Khoe, U.; Wang, X. M.; Horii, A.; Yokoi, H.; Zhang, S. G. *Nano Today* **2009**, *4*, 193–210.
(44) Sikorski, P.; Atkins, E. D.; Serpell, L. C. *Structure* **2003**, *11*, 915–926.
(45) Petkova, A. T.; Yau, W. M.; Tycko, R. *Biochemistry* **2006**, *45*, 498–512.

biomimetic assemblies but strikingly mimics the organization of hydrophobic proteins forming the walls of the gas vesicles of *Halobacterium halobium*.[34,35] Our system offers a unique opportunity to characterize biomimetic self-assemblies with molecular resolution, while gaining more insight into their molecular and supramolecular organization mechanisms. Indeed, lanreotide provides a favorable combination of several features: (i) the peptide is highly soluble, which was determined by its phase diagram yielding a critical nanotube concentration (CNC) as high as 21 mM;[46] (ii) both nucleation and elongation processes are fast, allowing studies at equilibrium; (iii) the molecular and supramolecular structure of the nanotubes is extremely well-ordered.[15] Hence, the lanreotide nanotube bundles is a remarkable model system for understanding the multiscale self-assembly processes in equilibrium conditions, which lead to only one among many metastable final structures via a series of identifiable steps. Here we show that an initial monomer to dimer equilibrium (K_d = 5 mM) occurs and is directly followed by the formation of stable open ribbons (15 mM) that are finally closed into nanotubes (21 mM) via an helical ribbon. These three sequential steps are delimited by two stable and one unstable intermediates that enforce a single pathway leading to a unique favored final molecular organization. Our description of the structural behavior of a biomimetic synthetic oligopeptide molecule addresses simultaneously the descriptive needs of structural biology with the architectural needs of current nanotechnology.

Experimental Section

Materials. Cyclic lanreotide (sequence NH_2-(D)Naph-Cys-Tyr-(D)Trp-Lys-Val-Cys-Thr-$CONH_2$; BIM 23014C) was obtained from Ipsen Pharma (Barcelona) as an acetate salt (molecular masses of 1,095 Da, purity >98%). Mixtures were prepared by dissolving the lyophilized peptide in pure water to raise the desired concentration. The samples were kept at room temperature, i.e. between 20 and 25 °C, for 24 h before measurements and electron microscopy observations. Tetraethyl orthosilicate (TEOS, purity > 99%) was purchased from Sigma and used as received.

Fluorescence Anisotropy Measurements. Fluorescence spectra were measured on a Spex Fluorolog 0.34 M spectrophotometer, equipped with a set of Glan-Thompson polarizers. Excitation and fluorescence spectra were collected using slit widths of 2 nm. To reduce scatter artifacts and to gain signal in fluorescence polarization measurements, a 280-nm filter was used instead of a slit for excitation and the emission slit width was changed to 10 nm. To remove the Raman scatter, spectra of distilled water were taken under the same conditions and subtracted. Because of the concentration, samples were all measured front-face to avoid inner filter effects.

Analytical Ultracentrifugation. Sedimentation Experiments. Experiments were performed at 20 °C on a Beckman-Coulter Optima XL-I analytical ultracentrifuge (Fullerton, CA) using an 8-hole-rotor AN-60 Ti and optical interference systems. Dried lanreotide peptide was diluted in deionized water. The same water was used as blank in the two-sector aluminum cells with sapphire windows (path length 1.2 cm).

Equilibrium Sedimentation. For each concentration, 10 optical interference scans were recorded for every speed and analyzed altogether with the software Origin (Microcal) using the theoretical distribution of the concentration of self-associating ideal species $c(r)$ versus the radial distance to the rotor axis r:

$$c(r) = \sum_{n=1-4} [(c_{\mathrm{mono},r_0})^n K_{a,n} \exp(nM(r^2 - r_0^2)(1 - \rho v\text{-}bar)\omega^2/RT)] + B \qquad (1)$$

where c_{mono,r_0} is the concentration of the monomer at the meniscus r_0, the number of subunits n, the association constant $K_{a,n}$ with $K_{a,1} = 1$ and $K_{a,n} = c_{n\text{-mer}}/[c_{\mathrm{mono}}]^n$), the specific partial volume $v\text{-}bar$, the solvent density ρ, the angular velocity ω, the gas constant R, the temperature T and the offset B. Variances between experimental points and best fits were used to select the models: single or self-associating species.

Sedimentation Velocity Experiments. Evaluation of the homogeneity of the peptide solution and the sedimentation coefficient s of molecular species were determined by processing sedimentation velocity experiments, two samples per run (300 μL). The sedimentation velocity profiles were scanned with the optical interference system every 4 min for a 1.21 mM solution of lanreotide at 60 krpm. We fitted theoretical boundaries from continuous discrete and non-interacting species on experimental data profiles with the software Sedfit[47] based on finite element solution of Lamm's equation and obtained a distribution of sedimentation coefficients $c(s)$ between 0.1 and 20 S. We used a confidence level of 0.95 for the regularization procedure. The frictional ratio f/f_0 was adjusted to recover theoretical MW or experimental values of the single molecular species weight measured by sedimentation equilibrium. The value of the hydrodynamic radius R_H was derived from the Svedberg equation: $s = M(1 - \rho v\text{-}bar)/(6\pi\eta R_H N_A)$, where N_A is Avogadro's number.

The lanreotide specific partial volume, theoretical molecular weight were computed from the protein sequence: $v\text{-}bar$ = 0.722 L/g, MW = 1095 Da, 1215 Da with counterions and ε^{280} = 6580 M^{-1} cm^{-1}. The solvent density ρ was estimated to be 1.001 g/mL, and the solvent viscosity η to be 0.001002 Pa·s.

^{1}H NMR Experiments. NMR experiments in 90% H_2O/10% D_2O were carried out at 20 °C on a DRX Bruker spectrometer operating at 500 MHz ^{1}H frequency, equipped with a X-^{1}H inverse probehead. Standard COSY, TOCSY, and NOESY spectra were recorded with mixing times of 70 ms (TOCSY) and 100−400 ms (NOESY) for the 1.4, 7.5, 14.6 mM peptide samples. For the ^{13}C chemical shift assignments, natural abundance ^{1}H−^{13}C HSQC spectra were recorded on the 1.4, 7.5, and 14.6 mM peptide samples. Water suppression was achieved using excitation sculpting.[48] Signal assignment was performed using the standard protocol.[49]

Transitional Diffusion Experiments by ^{1}H NMR. The translational diffusion experiments were performed on a 500 MHz BRUKER Avance II spectrometer equipped with a 5 mm HXN probehead and a BGU II gradient unit. The temperature was set to 293 K and checked with a methanol sample. The effective gradient strength was calibrated with water and cyclohexane samples.

The experiments were carried out at seven different concentrations ranging from 0.05 to 2% in H_2O/D_2O (95:5 v/v). The stimulated spin echo sequence[50] including bipolar gradients, spoil gradient, and water suppression via WATERGATE[51] was employed. To minimize the eddy current effects, sine-shaped gradients were used. For each peptide concentration, 16 experiments were performed with gradient strengths ranging from 19 to 306 mT/m at fixed intergradient delay Δ, to discard attenuation effects by relaxation. After Fourier transformation, manual phasing, and baseline correction, the peak at 0.86 ppm, corresponding to the methyl group of Val (Figure S1, Supporting Information), was

(46) Valery, C.; Artzner, F.; Robert, B.; Gulick, T.; Keller, G.; Grabielle-Madelmont, C.; Torres, M. L.; Cherif-Cheikh, R.; Paternostre, M. *Biophys. J.* **2004**, *86*, 2484–2501.

(47) Schuck, P. *Biophys. J.* **2000**, *78*, 1606–1619.

(48) Callihan, D.; West, J.; Kumar, S.; Schweitzer, B. I.; Logan, T. M. *J. Magn. Reson. Ser. B* **1996**, *112*, 82–85.

(49) Wüthrich, K. *NMR of Proteins and Nucleic Acids*; Wiley: New York, 1986.

(50) Boss, B. D.; Stejskal, E. O.; Ferry, J. D. *J. Phys. Chem.* **1967**, *71*, 1501.

(51) Piotto, M.; Saudek, V.; Sklenar, V. *J. Biomol. NMR* **1992**, *2*, 661–665.

integrated and used for the measured signal S, the signal (AU) at gradient strength G (in $T \cdot m^{-1}$); S_0 is the signal obtained with the lowest gradient strength (2 ms gradient length; 150 ms intergradient delay). The attenuation of the signal being proportional to $\exp(-G^2\gamma^2\delta^2(\Delta-\delta/3)D$, where γ is the gyromagnetic ratio and δ is the gradient length,[52] the slope of the curve $\ln(S_0/S) = f(G^2)$ gives access to the diffusion coefficient D.

According to the monomer−dimer equilibrium, the measured diffusion coefficients are averages of the diffusion coefficients for the pure monomer and the pure dimer, weighted by the molar fraction of the monomer in solution:

$$D_{\text{observed}} = x_{\text{mono}}D_{\text{mono}} + (1 - x_{\text{mono}})D_{\text{dimer}} \qquad (2)$$

Thus a multiparametric fit of the diffusion coefficients D_{observed} as a function of concentration against the theoretical equation enables extraction of D_{mono}, D_{dimer}, and the dissociation constant K_d. The shape of the equation is such that the extracted value for the dissociation constant bears a high uncertainty.

Electron Microscopy. During sample preparation for transmission electron microscopy (TEM), extreme care was taken to analyze and avoid any artifacts that could occur when using negative staining procedures. Indeed, we have previously showed the importance of electrostatic interactions in the self-assembly of lanreotide.[46] The use of salt staining solution could potentially induce aggregation and/or irrelevant self-assemblies. In order to discriminate the genuine lanreotide self-assembly intermediates from the possible stain-induced artifacts, samples were prepared using different staining approaches, and the corresponding electron micrographs were systematically compared. Therefore, classical negative staining using uranyl acetate, ammonium molybdate, methylamine vanadate, or sodium phosphotungstate was performed but also silica coating and glutaraldehyde fixation. The silica coating method is based on our previous work on the silica mineralization of lanreotide nanotubes.[53] We have demonstrated by Raman spectroscopy that the soft sol−gel mineralization does not alter the peptide organization within the nanotube walls. Finally, the glutaraldehyde fixation and replication technique allows the dilution of the samples while retaining the original architecture, whereas disassembly occurs when the sample is not chemically cross-linked. By comparing the electron micrographs obtained from the different sample preparations, we have observed the same architectures for all of the samples, thus confirming that our TEM observations provided a direct visual access to the actual intermediates of lanreotide self-assembly.

Negative Staining. The lanreotide solution was deposited onto freshly glow-discharged 400-mesh collodion/carbon-coated grids and allowed to settle for 1 min. Grids were then quickly blotted, briefly rinsed with distilled water and stained with different solutions. Uranyl acetate 2%, ammonium molybdate 1% and sodium phosphotungstate 2% are used as negative stains because of their high scattering power relative to biological molecules. Lower density materials such as methylamine vanadate (NanoVan) yielded a much smoother background than other stains, therefore enhancing the signal-to-noise ratio. In order to investigate whether the staining altered the final nanotube architecture, preliminary tests were performed with the different staining solutions on samples for which independent experiments (IR spectroscopy and small angle X-ray scattering) had shown that lanreotide nanotubes were readily formed. None of the staining methods induced such alteration.

Silica Coating. The silica replica of lanreotide open ribbons were obtained by the contact in a 1.5-mm diameter capillary of a 5% (w/w) gel and the pure TEOS liquid. The ribbons were found at the interface forming a macroscopic white ring and were aliquoted and suspended in ethanol. TEM observations were performed after the deposition of the suspension solution onto 300C-Holey Carbon grids covered with a thin carbon film.

Silica Staining-Replication. After observation of the silica staining grids, the same grids were Pt/C shadowed unidirectionally at an elevation angle of 45 °C.

Glutaraldehyde Fixation and Replication. A solution of 2.8% w/w lanreotide was mixed with a 2.5% glutaraldehyde solution (1:1 v/v). After an ultracentrifugation (1 h, 15 000 rpm), the supernatant was removed, and the pellet was resuspended in water. The suspension was deposited on a glow-discharged film coated with a collodion carbon film. The excess of solution was blotted with a filter paper, and the grid was dipped into liquid nitrogen. Frozen samples were transferred into a high-vacuum evaporator and maintained at −80 °C for 2 h for freeze-drying. Pt/C shadowing was performed unidirectionally at an elevation angle of 45°.

Observation of the Samples. Grids were observed with a Philips CM12 microscope operating at 80 kV.

Small Angle X-ray Scattering (SAXS). X-ray diffraction experiments were performed at the High Brilliance beamline (ID2), European Synchrotron Radiation Facility in Grenoble, France.[54] The undulator X-ray beam (of wavelength 0.99 Å) was selected by a channel-cut Si(111) crystal, and focused by rhodium-coated toroidal mirror. The circular beam size defined by the collimating slits was 0.2×0.2 mm^2. The detector was an image intensified charge-coupled device camera, and the sample-to-detector distance varied between 150 and 650 cm.

Results

Sequential 3-Step Assembly Process Driven by Peptide Concentration. The lower left panel of Figure 1 shows the evolution of the lanreotide fluorescence anisotropy with the peptide concentration (T = 25 °C). Lanreotide contains three aromatic residues, one of which, Trp, accounts for the entire peptide fluorescence.[55] Three regimes can be distinguished, a high fluorescence anisotropy state for concentrations between 15 and 21 mM and two low anisotropy states that are observed for less than 15 mM or more than 21 mM. The sharp increase for intermediate concentrations indicates that oligomeric architectures are formed. Indeed, in the absence of any energy transfer mechanism, oligomerization decreases the tumbling rate of the fluorescent molecules that in turn increases the measured anisotropy. The abrupt decrease for higher concentrations occurs at 21 mM, which is precisely the CNC previously determined.[46] Therefore, the low fluorescence anisotropy observed above 21 mM is due to an energy transfer between Trp within nanotubes as previously proposed.[55] Before the onset at 15 mM, large oligomers are not formed and the fluorescence anisotropy is consistently low. This experiment clearly points out a sequence of at least three major steps in the growth process as the concentration is increased, the intermediate one being attributed to high molecular weight lanreotide oligomers.

Spherical Dimer in Equilibrium with Monomers. In order to get further insight into the nature of the structures composing the low concentration regime, we run sedimentation experiments by analytical ultracentrifugation (AUC) at 20 °C with lanreotide solutions in the 0.7−14 mM concentration range (Figure 2a,b). This technique has been previously used in combination with other biophysical (different spectroscopies and structural approaches) to characterize the oligomerization of two peptides.[56]

(52) Stejskal, E. O.; Tanner, J. E. *J. Phys. Chem.* **1965**, *42*, 288–292.
(53) Pouget, E.; Dujardin, E.; Cavalier, A.; Moreac, A.; Valery, C.; Marchi-Artzner, V.; Weiss, T.; Renault, A.; Paternostre, M.; Artzner, F. *Nat. Mater.* **2007**, *6*, 434–439.
(54) Narayanan, T.; Diat, O.; Bosecke, P. *Nucl. Instrum. Methods Phys. Res., Sect. A* **2001**, *467*, 1005–1009.
(55) Pandit, A.; Fay, N.; Bordes, L.; Valery, C.; Cherif-Cheikh, R.; Robert, B.; Artzner, F.; Paternostre, M. *J. Pept. Sci.* **2008**, *14*, 66–75.

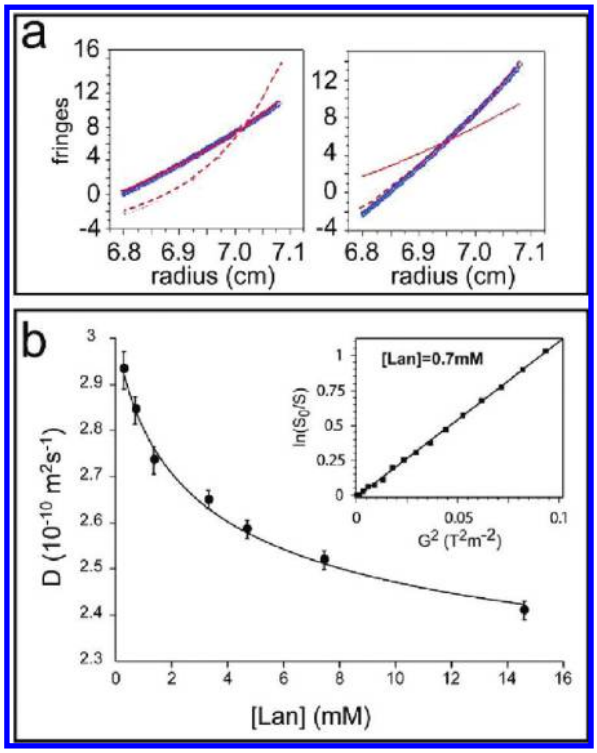

Figure 2. Analytical utracentrifugation and translational diffusion NMR experiments. (a) Equilibrium sedimentation profiles obtained at 20 °C for 1.2 (left panel) and 13.2 (right panel) mM of lanreotide in water. The blue curves represent the experimental profiles and the fits are represented in red. For both profiles we applied the two same models, i.e. a pure monomer specie (plain red lines) or a monomer−dimer equilibrium (dotted red lines). For the lowest lanreotide concentration solution only the monomeric model fits correctly the experimental data, whereas for the highest concentration the monomer−dimer give the best fit. The analysis gives molecular weights of 1230 and 2405 Da for the monomeric and dimeric species respectively. (b) Diffusion coefficients (in 10^{-10} m^2s^{-1}) extracted from ^{1}H NMR transitional diffusion experiments plotted as a function of the lanreotide concentration (in mM). Insert: the diffusion coefficients were extracted for each concentration from the slope of the linear relation $\ln(S_0/S) = f(G^2)$. The experimental curve presented was obtained for the sample at 0.7 mM peptide.

For interference scans recorded from 40,000 to 50,000 rpm, the best fits were obtained by considering a monomer with lanreotide concentrations comprised between 1.21 to 5.13 mM (monomer MW = 1230 Da/theoretical mass of the bis-acetate lanreotide-$C_{58}H_{77}N_{11}O_{14}S_2$- 1216 Da). For higher peptide concentrations, the best fits were given for a monomer−dimer equilibrium (dimer MW = 2405 Da/theoretical mass of the lanreotide dimer 2432 Da) yielding a dissociation constant, K_d, of 5 ± 1.0 mM. The coexisting molecular species in the different samples were identified by sedimentation velocity experiments, performed at 20 °C on peptide solutions in the same concentration range (Figure 3). The experimental interference optical scans were fitted with the theoretical boundaries of a continuous distribution of discrete and noninteracting species of the lanreotide as described by Schuck.[47] Below 5.13 mM, the sedimentation coefficient distribution, $c(s)$, corresponds to a single molecular species with a sedimentation coefficient at 20 °C and in water ($s_{20,w}$) of 0.488 S consistent with a monomer of theoretical MW = 1230 Da associated to a friction coefficient ratio f/f_0 = 1.10 (i.e., a slightly flattened sphere) (Figure 3C).

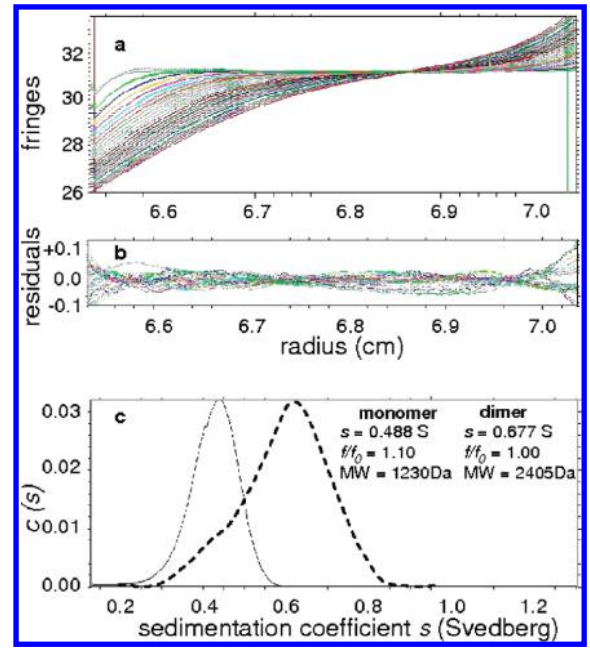

Figure 3. Analytical ultracentrifugation sedimentation velocity experiments. (a) Sedimentation velocity profiles scanned with the optical interference system every 4 min for 1.21 mM solution of lanreotide at 60krpm. (b) Residuals between the experimental data and the best fit. (c) Sedimentation coefficient distribution obtained for 1.21 mM (plain line) and 13.6 mM (dashed line) lanreotide solution.

For higher concentrations, the sedimentation coefficient distribution of the peptide shows a main peak at $s_{20,w}$ = 0.677 S corresponding to a peptide dimer of MW = 2405 Da with f/f_0 = 1.00 and a shoulder at 0.490 S (Figure 3C), suggesting the coexistence of monomers and dimers, in agreement with the equilibrium fluorescence experiments (Figure 1, left lower panel). Interestingly, the inferred friction ratio of 1.00 for the dimer supports the idea that the dimer shape can be well described by a sphere as expected for the face-to-face dimeric building block found in the nanotube structure (Figure 1b).[15]

The self-association of the lanreotide in dilute solutions was probed by the concentration dependence of the NMR spectra (i.e., 0.7−14.6 mM). Between 0.7 and 1.4 mM no major variation of the chemical shifts is observed, whereas at higher concentrations (7.5 and 14.6 mM) the changes in chemical shifts are likely due to the monomer−monomer interactions (Figure S1, Supporting Information). The presence of a single set of resonances for each proton present in the molecule indicates that the monomer and dimer states exchange rapidly on the NMR time scale in the 7.5 and 14.6 mM samples. This is in agreement with a symmetric dimer. NMR translational diffusion experiments were carried out at seven different concentrations ranging from 0.35 to 14.0 mM in order to reveal the effects of the peptide association on the translational diffusion (Figure 2c). Pulsed field gradient echoes enable the quantification of the diffusion coefficient D via the proton signal attenuation.[52,57] The experimental diffusion coefficients versus concentration plots were fitted assuming a monomer−dimer association model described in the Experimental Section. The translational diffusion coefficient of the pure monomer was found to be 3.00 ± 0.03 × 10^{-10} $m^2 \cdot s^{-1}$, which is consistent with the size of the peptide. Assuming a spherical shape for the dimer, as evidenced by sedimentation velocity experiments, the diffusion coefficient

(56) Goodman, J. L.; Petersson, E. J.; Daniels, D. S.; Qiu, J. X.; Schepartz, A. *J. Am. Chem. Soc.* **2007**, *129*, 14746–14751.

(57) Stilbs, P. *Prog. Nucl. Magn. Reson. Spectrosc.* **1987**, *19*, 1–45.

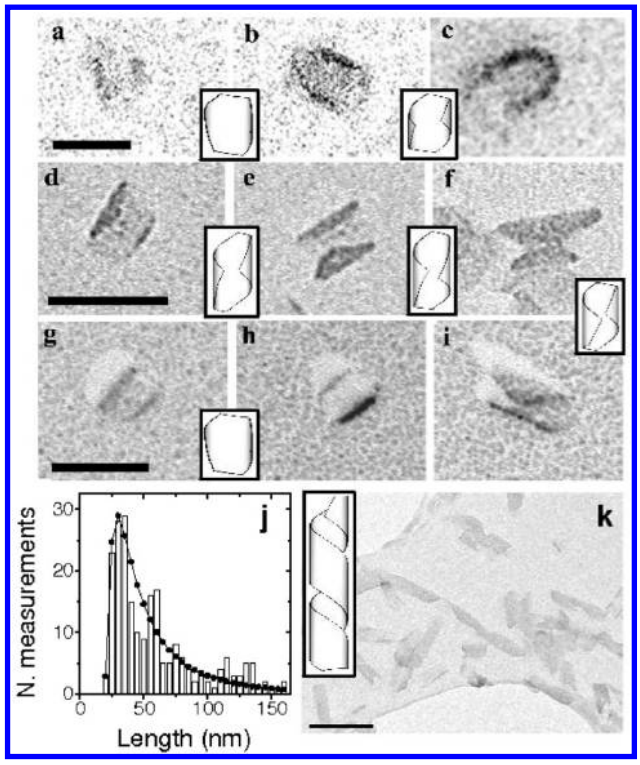

Figure 4. Open ribbons isolated by TEM. (a−c) Negatively stained open ribbons observed from a 19 mM lanreotide solution, illustrate different orientations of the ribbon on the supporting film. (d−f) Silica replicas of the open ribbon. (g−i) Silica replica of the open ribbons, observed after 45° Pt/C shadowing. Inserts: 3-D sketches of the intermediates to help the reader. (j) Histogram showing the length distribution of the open ribbons (225 measurements). (k) Electron micrographs of silica replicas of helical ribbons. Scale bar, 30 nm for panels a−i and 100 nm for panel k.

for the dimer, $2.12 \pm 0.07 \times 10^{-10}$ $m^2 \cdot s^{-1}$, corresponds to a mean diameter of 2 nm. This diameter is in very good agreement with the size of the face to face dimer building block of the nanotube wall structure.[15] The dissociation constant, $K_d = 5.3 \pm 1.8$ mM, is less precisely defined but is in full agreement with the dissociation constant estimated by AUC.

Higher Oligomerization of Lanreotide: Open Ribbons and Short Nanotubes. The nature of the structures responsible for the high fluorescence anisotropy was elucidated by performing transmission electron microscopy and SAXS experiments on lanreotide solutions as a function of concentration. For electron microscopy, different concentrations of between 15 and 20.3 mM have been characterized. Since lanreotide self-assembled structures are sensitive to variations of the ionic strength, different staining techniques and preparation methods have been applied and systematically compared in order to identify possible processing artifacts (see Experimental Section for details). On all of the micrographs, irrespective of which staining and preparation method, we have observed the coexistence of two types of objects, namely, small aggregates and short nanotubes, for concentrations from 16.8 to 20.3 mM. The proportion of small aggregates decreases in favor of short nanotubes as the peptide concentration increases (Figure S2, Supporting Information). Above 20.3 mM, nanotubes, several hundreds of micrometers in length, are exclusively observed.

In Figure 4, we focus on individual small aggregates for samples either stained with methylamine vanadate (Figure 4a−c) or sheathed with silica (Figure 4d−i). While negatively stained lanreotide solutions produce diffuse micrographs, we have recently demonstrated that silica interacts intimately with lanreotide during the nanotube growth and coats them without altering the molecular packing of the peptide. In those reported experimental conditions, (i) the mean diameter of the peptide nanotube was 24.4 nm before mineralization and 24.6 nm after silica deposition, and (ii) the Raman spectra of the pure lanreotide and silica-lanreotide nanotubes were identical.[53] In the present study, the silica-coated nanostructures are obtained under the same experimental conditions. This method presents at least two assets: (i) coated objects are encapsulated in a solid shell that stabilizes them and allows for their dispersion below the critical concentration, and (ii) silica-coated nanostructures are less prone to electron beam damage and do not need further staining since silica is providing a high enough contrast.

The 3-D morphology of the silica-coated objects can therefore be clearly revealed by shadowing them by angle evaporation of a thin metal film (Figure 4g−i). Indeed, some small aggregates appear to have a rectangular shape of homogeneous width (25 ± 3 nm) with two denser edges (Figure 4a,b,d). These edges are shown to be hemicircular or triangular protrusions upon shadowing (Figure 4a−d,g,h). Other aggregates more obviously exhibit refolded triangular sides in the TEM projections of Figures 4e, f, and i. Finally, Figure 4i clarifies the overall 3D morphology as being curved and open ribbons with beveled edges. The horseshoe-like shape of Figure 4c can thus be consistently understood as an axial view of a curved open ribbon. The set of electron micrographs obtained after the different staining and preparation methods consistently suggests the same 3-D morphology of the open ribbon, which is more easily inferred from Figure 4i. This consistency is a strong indication that the observed objects are neither generated nor modified by the sample preparation protocols, different staining, and preparation methods we used but reflect the genuine structure of the pretube intermediates. Furthermore, open ribbons show a constant width that is the nanotube final diameter,[15] but their length is markedly polydisperse as shown on the histogram in Figure 4j. The experimental length distribution can be fitted with a log-normal function, $f(X, x_0, s) = A^*\exp[-[\log(X) - \log(x_0)]^2/s^2]$, with $X = x - l_{min}$ (x being the ribbon length and l_{min} its minimal value), where x_0 is the average ribbon length and s is the standard deviation of the measurements.[58,59] The best fit results from the adjustment of s and l_{min} only and yields a most probable length of 30 nm and a minimal length l_{min} of 19 nm below which no aggregate is observed. Moreover, the open ribbons are terminated by sharp beveled edges, the angles of which are 20°, 40°, and 70°, with respect to the ribbon diameter (Figure 4; Figure S3, Supporting Information). These angles correspond to the reticular directions of the nanotube structure determined by Valery et al.[15] This morphological correspondence between the final organic template and the early stage structures along with the observation that nanotubes with filamentous or blurred tips were never observed despite a careful search point against the intuitive image of nanotubes made from twisted bundles of peptide filaments. Although we cannot formally exclude that interpretation, it seems more likely that the nanotube seeds consist of these curved open ribbons, which are the high molecular weight species that induce the sharp increase in the fluorescence anisotropy (Figure 1).

The abundance of the intermediates was investigated by a scattering technique in order to access volume information in solution without possible drying or staining artifacts. The small

(58) de Lamaestre, R. E.; Bernas, H. *Phys. Rev. B* **2006**, *73*.
(59) Limpert, E.; Stahel, W. A.; Abbt, M. *Bioscience* **2001**, *51*, 341–352.

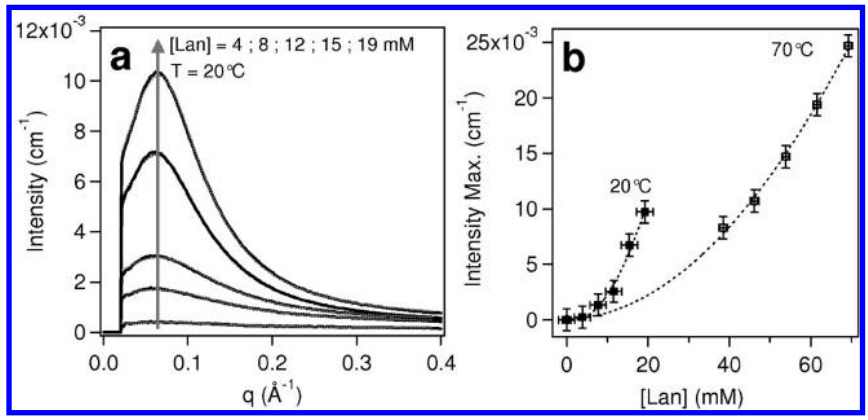

Figure 5. Open ribbons formation with concentration increase. (a) Small angle X-ray scattering of lanreotide solution at various concentrations at 20 °C. The arrow shows the increase of diffuse scattering with the concentration increase. Lorentzian fits are superimposed (dotted lines). The diffuse scattering position is constant with [Lan], $q_{max} = 0.064$ Å^{-1} (± 0.0015). The half-width at half-maximum (HWHM) decreases from 0.065 to 0.099 Å^{-1}. Note that similar SAXS patterns are observed at 70 °C, with a constant diffuse scattering position $q_{max} = 0.076$ Å^{-1} (± 0.002) and a HWHM decrease from 0.073 to 0.099 Å^{-1}. (b) The maximal diffused amplitude increases with [Lan] at 20 and 70 °C.

angle X-ray scattering study was conducted with various lanreotide concentrations at low and high temperature (Figure 5). All spectra can be well fitted by a single Lorentzian function (Figure 5a), which is characteristic of a liquid order with a short-range order. This liquid order, which decreases exponentially with the distance,[60] arises from dispersed entities with a mean interdistance of $2\pi/q_{max}$ that is independent of the concentration and decreases from 10 nm at 20 °C to 8 nm at 70 °C. The increase of the scattering intensities with the lanreotide concentration can not be accounted for by an increase of the number of scattering entities with the concentration since their mean interdistance is constant (Figure 5b). The only possible explanation is an increase of the form factor of the scattering entities with an augmentation of the number of scattered electrons per entity and consequently a size increase. The absence of any fluctuation of the scattering intensity is due to a broad polydispersity of entities shapes, in agreement with the size histogram extracted from the electron micrographs of the open ribbons (Figure 4j). It should be pointed out that when these open ribbons are formed, they are stable for days irrespective of the concentration or the temperature. The open ribbons correspond to the stable aggregates that were already detected in the phase diagram in a previous report.[46]

In extremely rare occasions that could be visualized upon silica staining, helical ribbons are visualized in coexistence with open ribbons and short nanotubes (Figure 4k). From this sample, the helical pitch length was measured to be 70 ± 20 nm (50 measurements), which is about twice the average length of the open ribbons and comparable to the observed maximal length of open ribbons (Figure 4j). Interestingly, since the β-sheet is coiled around the nanotubes with an angle of 41°,[15] the nominal helical pitch is $2\pi R \tan(41°) = 67$ nm, in very good agreement with our experimental estimate from TEM imaging. This further confirms that these objects are intermediates species in the nanotube growth albeit quite unstable as indicated by their scarcity.

Finally, below 20.3 mM, open ribbons coexist with short but closed nanotubes. Figure 6a−e (and Figure S2, Supporting Information) shows nanotubes that are shorter than those obtained above the critical concentration of nanotube formation.[46] In Figure 6a,b nanotubes of different size can be

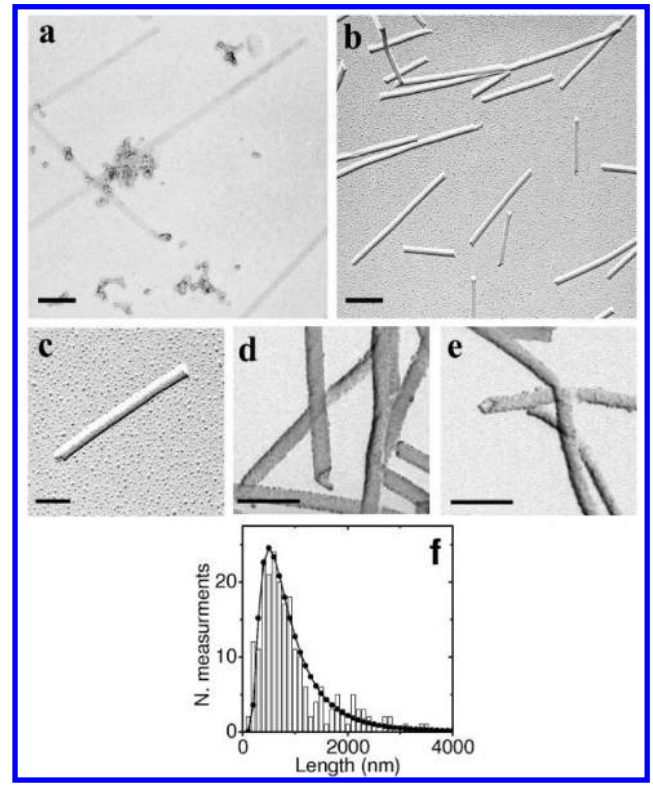

Figure 6. Short nanotubes. (a) TEM images of a lanreotide solution (2.7% w/w, i.e. 20.3 mM) stained with methylamine vanadate. (b−e) TEM images obtained after unidirectional shadowing by Pt/C of a lanreotide solution (2.8% w/w) pretreated with glutaraldehyde and diluted. Scale bar = 100 nm. (f) Histogram showing the length distribution of the short nanotubes (233 measurements). Scale bar, 100 nm.

observed, whereas in Figure 6c−e electron micrographs focused on the beveled extremity of the nanotubes. Similarly to open ribbons, the nanotube length distribution can be fitted with a log-normal function and shows that nanotubes have a minimal length of 100 nm (Figure 6f), which is substantially longer than the majority of the open ribbons (30 nm). High magnification electron micrographs of the nanotube ends (Figure S3, Supporting Information) do not reveal filaments but systematically beveled extremities, which exhibit the same 40° and 70° angles that coincide with the molecular packing within the crystalline wall of the nanotubes.

(60) Guinier, A. D. P. *X-Ray Diffraction in Crystals, Imperfect Crystals, and Amorphous Bodies*; Dover Publications: New York, 1994.

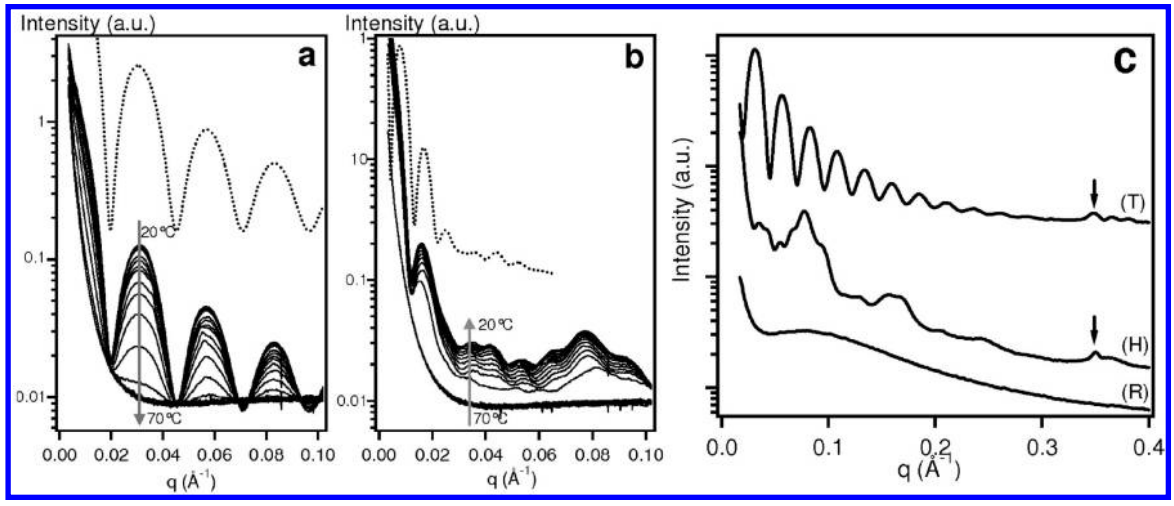

Figure 7. Nanotube dissociation-association cycle. Ultrasmall angle X-ray scattering of a lanreotide gel at [Lan] = 36 mM is recorded during a heating/cooling cycle between 20 and 71 °C (1 °C/min and 1 frame every 3 °C). Initially, at 20 °C, the sample is preheated at 70 °C and then cooled down to 20 °C and equilibrated for 24 h. (a) Initial diffuse scattering is well fitted by a Bessel function $[J_0(q \cdot r^\circ)/q]^2$ with r°= 122 Å (dotted lined). The diffuse scattering intensity decreases as the temperature increases (a) and vanishes at 50 °C. (b) Upon cooling, a complex diffuse scattering appears at 47 °C and increases upon further cooling. It can be well fitted (dotted line and see text). (c) SAXS collected at 71 °C (R), which are consistent with open ribbons, at 20 °C (H) after quenching as helical ribbons by rapid cooling, and at 20 °C (T) after 24 h equilibration and full reassembly of the tubes as in panel a.

Dynamic Studies of the Dissociation/Association of the Nanotubes. In order to complete this quasi-static study of the formation of the nanototube by increasing the concentration at fixed temperature, the knowledge of the phase diagram was exploited to study the dissociation/association of the nanotubes.[46] Indeed, between 21 and 70 mM, nanotubes can be melted by heating and reassembled by cooling. Therefore, full thermal cycles were explored by ultrasmall angle X-ray scattering. The initial scattering patterns corresponds to nanotube with monodisperse radius of 12.2 nm as previously observed.[15] The samples were rapidly brought to 70 °C and then cooled down at 0.5 °C/min to 20 °C for 24 h (Figure 7a and c, trace T). During the heating step (0.5 °C/min, Figure 7a), the nanotube characteristic spectrum disappears to generate a low scattering spectrum identical to the SAXS patterns obtained at 20 °C for low concentrations of lanreotide (Figure 5a). Figure 7b shows that an intense scattering appears at very small angle upon cooling that does not correspond to the nanotubes. This spectra can be fitted by a function $\cos^2(q \cdot p/2)\ \sin^2(q \cdot e/2)/q^2$ where $p = 71 \pm 3$ nm and $e = 20 \pm 2$ nm. The cosine factor is due to the pair interaction between two similar objects with an interdistance p,[19] and the sine factor is characteristic of a continuous object of width e.[60] Hence, the observed scattering reveals the 20-nm wide helical ribbons twisted with a 71-nm pitch. Hence, the pitch determined from the fit of the scattering patterns fits perfectly the one extracted from the electron micrographs on the helical intermediates. Moreover, considering the structure of the crystalline nanotube wall, there are three possible growth directions corresponding to the reticular directions of the crystal, 22°, 41°, and 75°. The pitch length of the helical ribbons can be calculated from these three angles (pitch length $=2\pi R \tan(\theta)$) and results in respectively 31, 67, 290 nm for the three possible growth directions. Only the growth direction following the H-bond network ($\theta = 41°$) gives a pitch length in agreement with our experiment. Furthermore, the presence of the 0.35 Å^{-1} peaks (Figure 7c) confirms a molecular packing identical to the one already demonstrated in the fully formed nanotubes. The comparison of the spectrum (R) in Figure 7c and the spectra of Figure 5a strongly supports that the melted species at 70 °C are the open ribbons. In conclusion, the dissociation of the nanotubes generates stable open ribbons. The association of the peptide onto these open ribbons by cooling produces helical ribbons that are stable more than 1 h but less than 24 h at 20 °C as they finally transform into nanotubes. This dynamical study confirms the sequence open ribbons, helical ribbons, nanotubes during the association process, and their stabilities.

Discussion: Nanotube Growth Mechanism. The sequence of successive equilibria that occurs during the lanreotide nanotubes formation has been evidenced by the observation of the different intermediate oligomeric species (Figure 8c): (i) monomer/dimer; (ii) dimer/open ribbons, (iii) open ribbons/short nanotubes. Two thermodynamically stable intermediates, the dimer and the open ribbons, have been identified and characterized.

The monomer/dimer equilibrium (i) was evidenced at 20 °C for lanreotide concentration up to 14 mM and is characterized by a dissociation constant, K_d of 5.3 ± 1.8 mM (Figure 8) leading to a Gibbs free energy of dimer dissociation per molecule ($\Delta_r G_d^{293K} = -1/2RT \ln[K_d^{293K}]$) as high as 6.6 kJ/mol. This high K_d implies a high solubility of the monomer and underlines the low efficiency of the peptide dimer formation. Indeed, besides the three aromatic amino acids that should drive the peptide dimerization thought hydrophobic interactions, lanreotide also possesses two positive charges that prevent the quantitative dimer formation by strong electrostatic repulsion. Nevertheless, when the open ribbons/short nanotube equilibrium is reached, i.e., for a total peptide concentration of 15 mM, 67% of the peptide is in its dimeric form, or in other words, the dimer: monomer species ratio reaches about 1:1.

Beside these energetic considerations, both analytical centrifugation and NMR experiments have independently demonstrated that the dimer can be assimilated to a 2-nm diameter sphere in good agreement with the characteristic size of the face-to-face dimeric building block derived from the nanotube structure. All together, these data strongly suggests that this first intermediate self-assembles at low concentration, persists throughout the peptide self-assembly pathway and is finally found as the elementary constituent of the resulting nanotube, the wall thickness of which is precisely set by the face-to-face dimer.

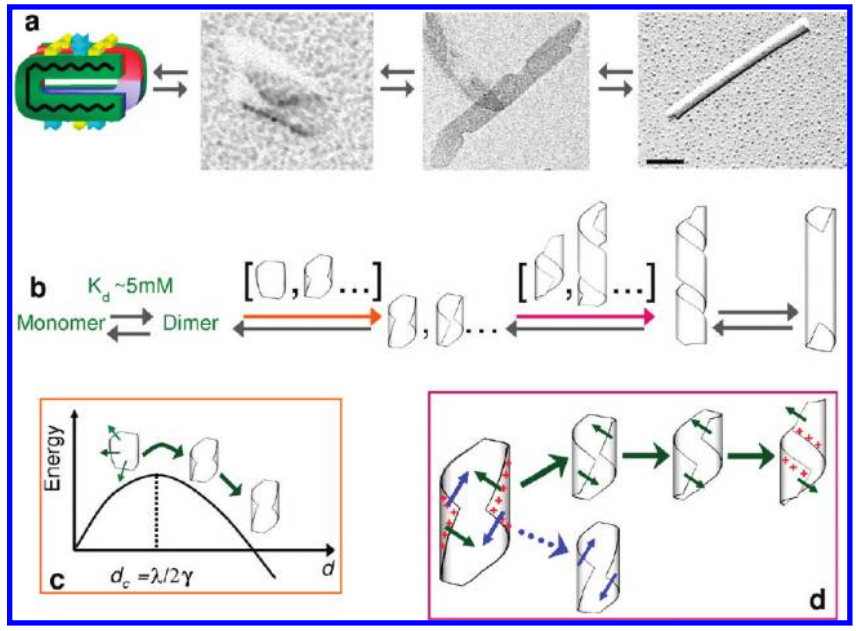

Figure 8. Nanotube formation: roadblocks and intermediates. (a) Scheme and images of the intermediates characterized in this work. (b) Intermediates and sequence of the nanotube self-assembly process. The formation of lanreotide nanotubes is described by a sequence of equilibriums between the different intermediate oligomeric species, i.e., monomer, dimer, open ribbons, helical ribbons, short nanotubes. (c) Nucleation and growth. 2-D crystal growth mechanism, i.e., nucleation and growth assembly and schematic evolution of the energy with the size of the nucleus that shows a typical "bell shape". The maximal energy is reached for d $=\lambda/2\gamma$, and smaller assemblies are not stable (see text for details). (d) Helical ribbons growing with electrostatic repulsions. When the edge of the open ribbons get closer, the repulsive forces favor one growth direction by slowing down the one that brings the edges of the ribbons to healing and closure. Among the two possible possibilities (either blue or green arrows), the system systematically growths along the green direction, i.e., the direction of the antiparallel β-sheet network, as proven by the pitch length of the helical ribbons (see text for details).

The SAXS scattering intensity of the open ribbons patterns plotted as a function of lanreotide concentration in Figure 5b is not linear. The inflection point evidenced at about 15 mM in agreement with the fluorescence data. Similarly, the open ribbons are detected by electron microscopy for lanreotide concentration exceeding 15 mM at 20 °C,. The combination of SAXS and TEM observations reveal that the open ribbons are curved 2D crystals, in which the octapeptide adopts the same molecular packing that is observed in the final nanotubes. The open ribbons and the final nanotubes have the same 24-nm diameter, the angles of the open ribbon edges correspond precisely to the reticular directions in the nanotube structure. Considering the known supramolecular structure of the nanotubes, two main routes for the formation of these curved ribbons can be envisioned (with or without intermediate filaments). First, in analogy to the microtubule formation, an initial unidirectional growth leading to long filaments is followed by a lateral stacking into wider ribbons. This process would produce protruding filaments as observed in TEM images of microtubules (9). However, such filaments have not been observed in the lanreotide structures, which suggest a direct 2D growth mechanism. Interestingly, no specific value prevails among the characteristic angles of the beveled open ribbons, suggesting that the dimers accretion has similar cohesion energies in the two reticular directions further supporting an isotropic growth of a 2D curved crystal.

The open ribbons length distribution (Figure 3j) can be fitted with a log-normal law with a minimal length of 19 nm. This onset can be understood by considering that the growth of a 2-D crystal nucleus is governed by two energetic terms. An interfacial energy gain results from the incorporation of dimers into the 2-D assembly, but this gain is moderated by the energy lost remaining at the edge of the crystal. The nuclei can be modeled as a 2-D plane crystal with a characteristic edge size d, and the surface and edge increase as d^2 and d, respectively. Hence, the total energy gain of a nucleus of size d can be written as $E = -\gamma d^2 + \lambda d$, with γ and λ being the surface energy of the 2D crystal and the linear energy of the edges, respectively. In Figure 6 (insert a), this very simple inverted parabolic evolution of the energy is plotted versus the size of the nucleus. The maximal energy is reached for $d_c = \lambda/2\gamma$, which implies that nuclei with $d < \lambda/2\gamma$ are unstable and disassemble back into dimers. Conversely, nuclei reaching a size $d > \lambda/2\gamma$ will be stable and able to minimize their energy by further growing. In agreement with this nucleation and growth process, these polydispersed yet stable nuclei are the ones visualized by electron microscopy, i.e., the open ribbons (Figure 4) and detected by SAXS (Figure 5). Therefore, the minimal length of the log-normal distribution reflects the energy barrier that lanreotide dimers need to overcome to produce open ribbons and sets the critical size at about 19 nm.

The observation of open ribbons in coexistence with short nanotubes suggests a transition state corresponding to the closure of open ribbons into nanotubes. This interpretation is further supported by the comparison of the length distributions of the open ribbons (Figure 4j) and short nanotubes (Figure 6f). Open ribbons longer than 30 nm are less frequent, and those exceeding 100 nm almost nonexistent, whereas dimers are still abundantly present in the solution. In contrast to classical nucleation and growth mechanism, this indicates another energy roadblock that interrupts the growth phase of the open ribbons. In parallel, short nanotube lengths follow a log-normal law with a minimal length of about 100 nm. It thus appears that curved ribbons grow in the open form until they reach an average length of 30 nm. An earlier closure of the open ribbons is prevented in our low ionic strength, nonscreening conditions (lanreotide is dissolved in pure water) by the mutual repulsion of the positive charges borne at

the intermediates angles (Figure 8). This constitutes the third roadblock along the pathway from lanreotide molecules to nanotubes.

The open ribbon/short tubes equilibrium is directly observable on TEM images where both species are seen to coexist (Figure S2, Supporting Information). The further growth of open ribbons can, in principle, lead to two possible situations. If the open ribbons keep on growing similarly in the two reticular directions, the final structure should have a "rolled-up carpet" morphology as reported for multilamellar vesicles in polar lipid systems, for example. However, this would imply that the gyred lamellae can accommodate a varying curvature radius, which is in contradiction with the observation that the curvature radius remains constant from the open ribbon stage until the final nanotubes. Also the known structure of fully formed nanotubes is incompatible with the gyred lamellae morphology. Alternatively, if the open ribbons proceed to a unidirectional growth, through either the H-bonding or the hydrophobic interactions axis (Figure 8), helical ribbons would be obtained. Furtermore, these helical ribbons would result into nanotubes by seamlessly closing the gap with or without the ultimate insertion of dimers. The rare TEM images of the elusive intermediates are a strong indication in favor of the helical ribbons (Figure 3k). These helical ribbons suggest that the second mechanism is the correct one: the initially isotropic growth of open ribbons then proceeds to a uniaxial extension. Incidentally, the observed helical ribbons also refute the scheme where the open ribbon first closes and then grows uniaxially as a closed tube of increasing length. It is most likely that the addition of the last dimer between the two tips of the beveled edges required for the closing of the short open ribbons is energetically forbidden due to the strong repulsive electrostatic forces generated locally by the protonated amine groups. Instead, the system increases the edge length by growing along one dimension. The two resulting parallel edges are eventually seamlessly closed.

The definitive confirmation of the mechanism proposed in Figure 8 comes from disassembly−reassembly experiments performed by SAXS measurements. Indeed, the concentration/temperature phase diagram[46] established few years ago shows that the nanotubes are formed when the total concentration of peptide reaches a critical concentration (CNC) and that this CNC is temperature-dependent. The CNC increases with temperature, indicating that the self-assembly process is driven by enthalpy more than by entropy (the CNC should have decreased with temperature in this last case). Second, when diluted, the amount of nanotubes progressively decreases and disappears when the total peptide concentration reaches below the CNC. Finally, SAXS patterns recorded during a heating (from 20 to 71 °C, Figure 7a)−cooling (71 to 20 °C, Figure 7b) cycle at a rate of 1 °C/min show that the nanotube disappears during the heating in favor of polydispersed aggregates that correspond to the open ribbons (Figure 7a). Upon cooling, a strong scattering pattern appears that can be fitted by a helical ribbon 20 nm in width and turning with a pitch length of 71 nm, this pitch length corresponding to the one measured on the electron micrographs on the helical intermediates. These helical ribbons are slowly transformed into closed nanotubes. Therefore these experiments definitely evidence the intermediates characterized by TEM using negative staining, silica coating, and gluteraldehyde fixation. Moreover, they rule any other pathway for the formation of lanreotide nanotubes. Moreover, whatever the thermal treatments (high (71 °C) or low (20 °C) temperatures), as soon as the system is set back to 20 °C, the nanotubes are reformed within less than 24 h with the same monodispersity and diameter as the ones self-assembled initially, thus proving the full reversibility of the system.

The seamless bonding of helical ribbons into closed nanotubes has been seen for lipids nanotubes such as diacetylenic phospholipid-based tubules[61] or cationic amphiphiles interacting with chiral counterions.[18] Only a few cases of peptide helical ribbons closing into nanotubes have been reported. One remarkable example is the closure of coiled ribbons into monodispersed nanotubes for the seven-residue peptide Aβ(16-22), CH_3CO-KLVFFAE-NH_2.[62] However, these helical ribbons were built from the lamination of fibrils and not from a curved 2-D crystal growing by successive dimer addition as in the present case.

Conclusion

We have shown that the self-assembly of lanreotide nanotubes follows a three-stepped route marked by successive energy roadblocks, namely, the peptide dimerization, the open ribbon growth up to the critical size, and the nanotube closure. Indeed, a dimeric building block is formed at low concentration from a balance between attractive hydrophobic interactions and repulsive electrostatic forces due to the two positive charges of the peptide. Higher oligomeric species, open ribbons, are formed above a critical concentration but remain stable only when their size exceeds a critical value of about 19 nm. Open ribbons are rigid 2-D crystals with an intrinsic curvature that most probably results from the expression of the molecular chirality and defines the nanotube diameter at the onset of the self-assembly process. Open ribbons coexist in equilibrium with short nanotubes through an unstable intermediate that has been identified as a helical ribbon that is subsequently seamlessly healed into a nanotube. The nanotubes then proceed to an unrestricted longitudinal growth to attain lengths of a few hundred micrometers. The route followed by lanreotide from the open ribbon to the nanotube is controlled by electrostatic repulsion. The most remarkable feature of the lanreotide system is that two of the three size features of the nanotubes are determined by the earliest generated supramolecular species. The nanotube diameter is set by the intrinsic curvature of the 2D open ribbons, and the wall thickness results directly from the dimerization. This study therefore thoroughly elucidates the mechanism of the lanreotide self-assembly into well-defined nanotubes, and the funnel concept, which was introduced for protein folding[63] and later on successfully used to describe the binding behavior in proteins,[64] seems to apply also to large macromolecular complex folding such as ribosomes[65] or, in our case, to the 26-fold-axis symmetrical self-assembly of a short octapeptide. It thus appears that the spontaneous emergence of such well-defined complex and multiscale supramolecular architecture is strongly enhanced when the formation route is punctuated with stable milestone states, each of them preparing the next assembly step. Furthermore, this precise and unequivocal self-assembly process is driven by the subtle balance between van der Waals attractive and repulsive electrostatic forces.

(61) Singh, A.; Wong, E. M.; Schnur, J. M. *Langmuir* **2003**, *19*, 1888–1898.
(62) Lu, K.; Jacob, J.; Thiyagarajan, P.; Conticello, V. P.; Lynn, D. G. *J. Am. Chem. Soc.* **2003**, *125*, 6391–6393.
(63) Bryngelson, J. D.; Wolynes, P. G. *J. Phys. Chem.* **1989**, *93*, 6902–6915.
(64) Tsai, C. J.; Kumar, S.; Ma, B. Y.; Nussinov, R. *Protein Sci.* **1999**, *8*, 1181–1190.
(65) Talkington, M. W. T.; Siuzdak, G.; Williamson, J. R. *Nature* **2005**, *438*, 628–632.

Our findings suggest that the rational design of oligopeptides can encode both molecular- and macro-scale morphological characteristics of their higher-order assemblies thus opening the way to ultrahigh resolution peptide scaffold engineering.

Acknowledgment. This work has been supported by the Agence Nationale pour la Recherche (project THERA-PEP/2005) and the French Ministry of research (Ph.D. thesis of E.P.). Theyencheri Narayanan is acknowledged for high quality of assistance during the Synchrotron X-ray experience and ESRF for beamtime allocation. We are grateful to Dr. J.-M. Verbavatz for the preliminary electron micrographs of lanreotide solutions and to Dr. C. Ebel for helpful discussions that convinced us to perform analytical centrifugation.

Supporting Information Available: 1-D ^{1}H NMR spectra of lanreotide solution at different concentrations, electron micrographs showing the coexistence of open ribbons and short nanotubes, and angle measurements of the beveled edges of the open ribbons and of the ends of the short nanotubes. This material is available free of charge via the Internet at http://pubs.acs.org.

JA9088023